RSC Advances

PAPER

Cite this: *RSC Adv.*, 2016, **6**, 77329

Novel one-pot synthesis and sensitisation of new BiOCl–Bi_2S_3 nanostructures from DES medium displaying high photocatalytic activity†

V. C. Ferreira,*[a] M. C. Neves,[b] A. R. Hillman[c] and O. C. Monteiro[a]

Received 3rd June 2016
Accepted 8th August 2016

DOI: 10.1039/c6ra14474h

www.rsc.org/advances

A novel route to synthesise Bi_2S_3-sensitised BiOCl nanoparticles from deep eutectic solvent medium at room temperature by a one-pot approach is reported. The influence of the temperature, sulphur source, concentration of reactants and presence of water, on the morphological, structural and microstructural, optical and photocatalytic properties of the synthesised nanoparticles is analysed and discussed. Stable and crystalline BiOCl hybrid structures with shapes from sheet-like to flower-like hierarchical aggregates and (001) and (110) dominant crystallographic orientation were obtained. The sensitisation of BiOCl with Bi_2S_3 was successfully achieved *in situ* during synthesis by an ion-exchange process and the relative proportion of the components (BiOCl and Bi_2S_3) was controlled by the Bi : S ratio in the synthesis medium and by the sulphur precursor. The sensitiser nanomaterial (Bi_2S_3) extends the BiOCl photoactive region to the visible range. Also it favours charge separation and reducing the electron/hole pair recombination and therefore increasing the photocatalytic performance. The prepared composite materials show high ability to adsorb rhodamine B cationic dye and the complete photocatalytic degradation was achieved within 45 min (75 mg per g of catalyst).

Introduction

Bismuth oxychloride (BiOCl) has recently attracted increasing interest due to its low toxicity, semiconducting properties, excellent photocatalytic response and versatility to be further modified with a wide range of materials. In the last decade, more than 190 research papers have been published only regarding BiOCl and its composites synthesis, properties and applications. It is their size, shape and surface structure which will, ultimately, control their optical and photocatalytic properties and therefore their suitability to distinct purposes. For example, BiOCl has shown ability for the water splitting reaction under solar light irradiation,[1–3] photocatalytic activity for the degradation of dyes and other pollutants under ultra-violet (UV) and visible radiation,[4–11] as UV photodetectors,[12] to be used as a catalyst, to be used as the air electrode of aluminium–air batteries[13] and as an anode material for sodium-ion batteries.[14]

BiOCl has a tetragonal structure, formed by layers of $[Bi_2O_2]^{2+}$ intercalated with a double layer of chloride ions accommodated in the interlayers, with interlayer distance of 7.38 Å. Due to its layered structure this material can be prepared in a wide range of sizes and shapes, with sheet and plate-like morphologies the most commonly reported,[5–7,10,14–16] however hexagonal prisms[8] and hierarchical structures resulting from distinct assembling of nanosheets are also reported.[4,7,9,11] BiOCl is a semiconductor with wide band gap and indirect band gap energy (E_g). Values ranging from 2.25 to 3.5 eV have been reported in the literature,[1,2,4,6,9,10,17] depending mostly on particle size, crystal structure and surface composition.

The synthesis methodologies of BiOCl are mostly based on hydro/solvothermal approaches and precipitation, but ultrasound assisted and combustion methods are also reported. Typical hydro/solvothermal based approaches require moderate to high temperatures (80–200 °C), often extended reaction times (12–24 h) and the use of specific reaction vessels.[4–6,9,11,14] The precipitation at room temperature, the synthesis assisted by ultrasound and the combustion methods requires subsequent calcination at 300–400 °C.[15,18,19]

In order to increase the photocatalytic performance and extend the absorption to the visible range, several strategies have been used in order to improve the efficiency of semiconductor photocatalysts, for example by controlling crystal facets, doping, organic and inorganic sensitisation, and preparation of hybrid structures. It has been shown that the photocatalytic activity of BiOCl depends not only on its particle dimensions but also on the crystallographic orientation of its surface.[5,6,10] BiOCl nanoplates with high exposed (001) facets

[a]*Centro de Química e Bioquímica, Faculdade de Ciências, Universidade de Lisboa, 1749-016 Lisboa, Portugal. E-mail: vcferreira@fc.ul.pt; Fax: +351 217500088; Tel: +351 217500000*

[b]*CICECO, Department of Chemistry, University of Aveiro, 3810-193 Aveiro, Portugal*

[c]*Chemistry Department, University of Leicester, University Road, Leicester, LE1 7RH, UK*

† Electronic supplementary information (ESI) available: Pictures of samples, TEM images and XRD diffraction patterns. See DOI: 10.1039/c6ra14474h

show enhanced activity towards methyl orange (MO) degradation under simulated sunlight irradiation.[5] Also BiOCl single crystalline nanosheets with exposed (001) facets present high photocatalytic activity for MO degradation through direct BiOCl photoexcitation under UV irradiation whereas nanosheets displaying (010) crystallographic orientation are more active to dye degradation through indirect dye photosensitisation under visible light.[6] Jiang *et al.*[1] have reported sulphide (S^{2-}) doping of BiOCl by replacing the chloride ions by S^{2-} in the interlayer. This widens the light absorption and decreases the band gap by 0.2 eV by creating impurity states just above the valence band. This allows those materials to be used for the oxygen evolution reaction due to extension of light absorption to the visible and improved separation efficiency of the photogenerated electron–hole pairs. Ding *et al.*[20] have shown that replacing Bi atoms in the crystalline structure by doping BiOCl with Er^{3+} (1%), allows the use of visible light and confers it catalytic properties towards rhodamine B (RhB) degradation. Owing to its high ability to adsorb some organic molecules, BiOCl has been sensitised with the organic dye RhB displaying enhanced photocatalytic activity towards the MO, 4-chlorophenol and nitric monoxide degradation under visible light irradiation.[11,21] The sensitisation with other inorganic materials such as SnO_2, Co_3O_4, WO_3, Fe_3O_4, Bi_2O_3, Bi_2S_3 and Bi has also been reported.[16,17,22–27] Of those, bismuth sulphide (Bi_2S_3) may be a suitable candidate since it displays photocatalytic activity towards dyes degradation under UV light irradiation.[28] Cao *et al.*[25] and Cheng *et al.*[27] have used a two-step process to prepare the BiOCl nanostructures and further sensitise with Bi_2S_3 through an ion exchange method using thioacetamide, thiourea and cysteine as sulphur precursors. This approach shows advantages over other methodologies reported in the past in which high reaction temperature, capping agents and use of less environmentally friendly reactants were required.[29–32] The presence of Bi_2S_3, which has a band gap energy in the range 1.2 to 1.8 eV,[26,33–35] extends the absorption of the hybrid material to the visible region since BiOCl only absorbs in the UV ($E_{g\ BiOCl\ bulk} = 3.5$ eV). The BiOCl/Bi_2S_3 nanomaterials exhibit efficient visible light photocatalytic activity towards RhB, 2,4-dichlorophenol and MO degradation processes.[25–27]

Considering all the efforts reported in the literature, the development of rapid strategies to prepare heterostructures displaying improved properties is still highly desirable and a challenge to which this work aims to contribute. Therefore, in this work, hybrid materials, with improved properties for photocatalytic applications, based on bismuth(III) oxychloride sensitised with bismuth sulphide semiconductor have been investigated. The novel approach reported here involves the one-pot synthesis and *in situ* sensitisation, by an ion exchange route. The ability of using environmentally friendly medium such as the deep eutectic solvent based on choline chloride and ethylene glycol and the synthesis at room temperature, in a one-pot reaction method presents further advantages.

The work reported here is distinct from that reported in the cited literature[25–27] in several respects, namely (i) the synthesis and sensitisation is achieved in an single step at room temperature; (ii) the hierarchical nanostructures are obtained from an environmentally friendly solvent and (iii) the resulting hybrid materials display significantly improved photocatalytic response.

The photocatalytic performance of the prepared BiOCl–Bi_2S_3 hybrid materials was studied and the results indicated that these are promising materials for application as catalysts for photocatalytic degradation of pollutants, such as (but not limited to) organic dyes.

Experimental

Materials and methods

All reagents were of analytical grade (Aldrich and Fluka) and were used as received. The aqueous solutions were prepared with Millipore Milli-Q ultra-pure water.

BiOCl–Bi_2S_3 nanoparticles synthesis. The BiOCl–Bi_2S_3 nanoparticles were chemically synthesised in a deep eutectic solvent (DES) medium prepared from a mixture of a 1 : 2 ratio of choline chloride and ethylene glycol (ChCl : 2EG).[36] Two bismuth sources were used, saturated solution of bismuth(III) trichloride ($BiCl_3$) in HCl and bismuth(III) diethyl-dithiocarbamate complex ($Bi[S_2CN(C_2H_5)_2]_3$,[37] $Bi(dtc)_3$) synthetised according to the procedure reported in the literature.[33] The sulphur sources tested were saturated aqueous solutions of sodium thiosulfate ($Na_2S_2O_3$, 3.2 mol dm^{-3}) and sodium disulphide (Na_2S, 2.4 mol dm^{-3}). The bismuth(III) diethyl-dithiocarbamate complex (Bi$[S_2CN(C_2H_5)_2]_3$) already contain both Bi and S and no extra sulphur source is required. Stock DES solutions of the precursors, $BiCl_3$ (16 mmol dm^{-3}), $Na_2S_2O_3$ (21 mmol dm^{-3}) and Na_2S (10 mmol dm^{-3}), were prepared by stirring until clear solutions were obtained. Typically for the BiOCl–Bi_2S_3 synthesis, to 20 mL of $BiCl_3$ stock solution, adequate volume of sulphur precursor solution was added under stirring. The reaction was allowed to occur overnight, at room temperature. Reactants concentration, temperature and sulphur source influences the time elapsed for change in the solution colour from clear to yellow, light brown and finally dark grey/black. After synthesis, the resulting suspensions were centrifuged at 3500 rpm for 5 minutes and the solid repeatedly washed with deionized water. The resulting solids were dried and stored.

White bismuth oxychloride (BiOCl) particles were obtained by adding the $BiCl_3$ saturated solution to H_2O;[25] bismuth sulphide (nanoBi_2S_3) was prepared according to the procedure previously described.[33]

The prepared samples are designated, according to Table 1, from A to E followed by the proportion of Bi : S in the starting reactants using $Na_2S_2O_3$ as sulphur source, *e.g.* A (1.5 : 1). Samples F and G were respectively prepared with (3 : 1) Bi : S proportion from another sulphur source (sodium sulphide – SS) and a bismuth(III) diethyl-dithiocarbamate complex (DT/50) already containing Bi and S in the proportion (1 : 6), both prepared at 50 °C. Thiourea (TU), thioacetamide (TA) and carbon disulphide (CD) were also tested but no particles were obtained. Furthermore, BiOCl/Bi_2S_3 particles, samples K and L, were also prepared using dry $BiCl_3$ and $Na_2S_2O_3$ directly dissolved in DES, in the proportion (1 : 3) and (1 : 4), respectively.

Table 1 Experimental conditions used for the synthesis of BiOCl–Bi_2S_3, BiOCl and nanoBi_2S_3 particles

Sample	Precursors	Bi : S	Conditions
A	$BiCl_3/Na_2S_2O_3$[a]	(1.5 : 1)	Room temperature, overnight, DES
B		(1 : 1)	
C		(1 : 1.5)	
D		(1 : 2)	
E		(1 : 3)	
F (SS/50)	$BiCl_3/Na_2S$[a]	(3 : 1)	50 °C, overnight, DES
G (DT/50)	$Bi(dtc)_3$	(1 : 6)	
H (TU)	$BiCl_3$/thiourea	(1 : 2)	50 °C, overnight, DES
I (TA)	$BiCl_3$/thioacetamide	(1 : 2)	
J (CD)	$BiCl_3/CS_2$	(1 : 4)	
K	$BiCl_3/Na_2S_2O_3$[b]	(1 : 2)	Room temperature, overnight, DES
L		(1 : 4)	
BiOCl	$BiCl_3$	—	Room temperature, H_2O
nanoBi_2S_3	$Bi(dtc)_3$	—	Acetone, 60 °C

[a] From saturated aqueous solutions. [b] From dry precursors.

Characterization

X-ray powder diffraction (XRD) was performed using a Philips X-ray diffractometer (PW 1730) with automatic data acquisition (APD Philips v3.6B), using Cu K_α radiation ($\lambda = 0.15406$ nm) and working at 40 kV/30 mA. The diffraction patterns were collected in the range $2\theta = 8$–$60°$ with a 0.02° step size and an acquisition time of 2.0 s per step. Optical characterization of the powder samples was carried out by UV-vis diffuse reflectance using a Shimadzu UV-2600PC spectrophotometer. Diffuse reflectance spectra (DRS) were recorded in the wavelength range of 200–1400 nm using an ISR 2600Plus integration sphere. Transmission electron microscopy (TEM) and high resolution transmission electron microscopy (HRTEM) were carried out using a JEOL 200CX microscope operating at 200 kV and scanning electron microscopy (SEM) in a field emission gun – scanning electron microscope JEOL-7001F (FEG-SEM), operating at 10–15 kV. Specific surface area was estimated by the Brunauer–Emmett–Teller (BET) method, from nitrogen (Air Liquide, 99.999%) adsorption data at −196 °C, using a volumetric apparatus from Quantachrome mod. NOVA 2200e. The samples, weighing between 40 and 60 mg, were previously degassed for 2.5 h at 150 °C at a pressure lower than 0.133 Pa. The potential of zero charge (p.z.c.) of the particles was measured using a Zetasizer Nano ZS90 (Malvern Instruments Ltd., UK), equipped with He–Ne laser (4 mW, 632.8 nm) using aqueous 0.1 M HCl and NaOH solutions for pH adjustments.

Adsorption and photocatalytic activity

All photocatalytic experiments were conducted using the procedure described elsewhere.[38] Briefly, a 250 mL refrigerated photoreactor using a 450 W Hanovia medium pressure mercury-vapour lamp was used as radiation source. The total irradiated energy was 40–48% in the ultraviolet range and 40–43% in the visible region of the electromagnetic spectrum. Prior to irradiation, 20 mg of sample were suspended in 150 mL of a rhodamine B solution (10 ppm) and were stirred in dark conditions during 60 minutes to allow the adsorption/desorption equilibrium. After this time an aliquot of solution was collected to evaluate the adsorption of RhB on the catalyst and used as $t = 0$ for the photocatalytic degradation. During irradiation, aliquots of the suspensions were collected at regular intervals using a peristaltic pump, centrifuged and analysed by UV-vis spectroscopy.

Results and discussion

Structural and morphological characterisation

Effect of the bismuth : sulphur ratio. Fig. 1 illustrates the X-ray diffraction patterns obtained for the A–E as-prepared samples. The peaks in the diffraction patterns can be indexed to the tetragonal crystallographic structure of BiOCl (ICDD PDF4 file: 01-085-0861) and agrees with the pattern obtained for the BiOCl synthesised from aqueous medium. The structure of BiOCl comprises layers of $[Bi_2O_2][Cl_m]$ or $[Bi_3O_{4+n}][Cl_m]$, with the chloride ions in a non-bonding interaction in the interlayers, this arrangement being prone to form 2D lamellar particles.[7] Sample A (1.5 : 1) shows higher crystallinity in opposition to the one of sample E (1 : 3) suggesting that the increase of the S content in the synthesis medium affects the crystallinity of the final particulates. Particles A (1.5 : 1), B (1 : 1) and C (1 : 1.5) clearly display preferential crystallographic orientation, with the peaks at 12.0° ((001) facets) and 32.5° ((110) facets) exhibiting higher relative intensities than those reported for bulk BiOCl (ICDD PDF4 file: 01-085-0861). This is further confirmed by the high relative intensities observed for the diffraction peaks of the same family of (001) facets, (002) and (003). Therefore the nanoparticle surface is dominated by (001) and (110) facets. Once BiOCl is predisposed to form 2D structures due to its lamellar nature, it is likely that faces of the particles comprise (001) facets while the edges are formed by (110) facets, in agreement with data previously reported.[6]

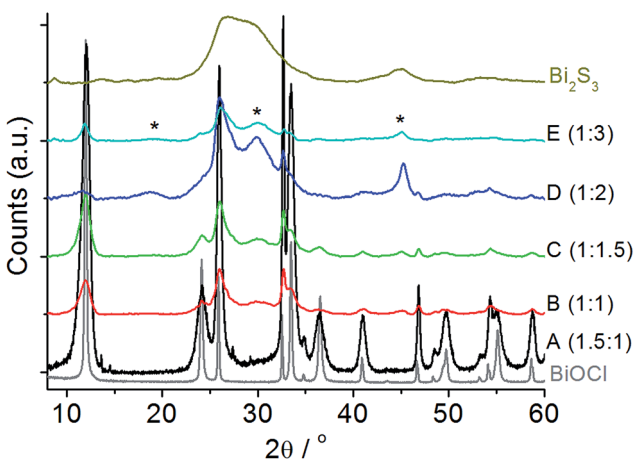

Fig. 1 XRD patterns of samples A (1.5 : 1), B (1 : 1), C (1 : 1.5), D (1 : 2) and E (1 : 3) and of pure BiOCl and nanoBi_2S_3.

Additional diffraction peaks were detected, in samples B to E, at 18.8, 30.0 and 45.2°, which can be assigned to the Bi_2S_3 facets (210), (100) and (214), respectively, (ICDD PDF4 file: 04-012-0700). Besides, other Bi_2S_3 diffraction peaks are likely to be overlaid with BiOCl signal (at about 23.8, 26.0, 33.4, 41.2, 46.6, 49.7 and 55.1°). The presence of nanocrystalline Bi_2S_3 seems to be a consequence of the sensitisation of BiOCl particles during synthesis in the presence of an appropriate sulphur source, for instance $Na_2S_2O_3$. This process is very likely to occur through an ion exchange process as it has been previously observed,[25–27] in heterostructures prepared in a stepwise approach. In the present case, the Bi_2S_3 sensitisation extension increases with the S content in the reaction medium. The aforementioned diffraction peaks are not detected for sample A most probably due to its dispersity and low Bi_2S_3 content. However, the formation of black particles, not white as pure BiOCl, suggests effective sensitisation. Upon synthesis of the NPs, it was clear that all the synthesised particles were not pure BiOCl (ESI, Fig. S1†) as their colour is very distinct from the white pure BiOCl.[25,39] The hypothesis of the synthesised particles containing sulphur atoms, as dopant replacing Cl^- ions in the interlayers, was discarded since a shift towards lower 2θ values would be expected due to the high atomic radius of sulphur atoms as compared with chloride ion and to difficulties in accommodating di-anions (S^{2-}). Also the hypothesis of incorporation of sulphur replacing oxygen atoms in the crystalline structure of BiOCl was rejected. This would cause expansion and/or distortion of the crystalline structure and concomitant shift of diffraction peaks towards lower 2θ values due to a similar effect as mentioned above, which was not observed.

The influence of the sulphur precursor. The X-ray diffraction patterns for samples F (SS/50) and G (DC/50), both prepared at 50 °C (no particles were formed at room temperature) and using Na_2S and $Bi(dtc)_3$ complex as sulphur sources, respectively, are shown in Fig. 2. Those patterns are similarly composed of BiOCl, displaying good crystallinity and preferential crystallographic orientation as observed for samples A to C.

However, using the $Bi(dtc)_3$ precursor, the yield is very low and particles with heterogeneous morphology were obtained, comprising large, irregular and thin flakes of BiOCl, of about 2 μm wide, mixed with small irregular particles (ESI, Fig. S2†). For that reason this sample was not used for further studies.

Other sulphur sources and the effect of H_2O. Under the experimental conditions used, no particles were obtained from DES using thiourea, thioacetamide and carbon disulphide as sulphur source, neither at room temperature or at 50 °C, indicating that the S precursor plays an important role on the final product and in the formation of particles by one-pot BiOCl synthesis and sensitisation.

In order to test the effect of water on the reaction medium, $BiCl_3$ and $Na_2S_2O_3$ were dissolved directly in the DES, instead of using saturated aqueous solutions. Under these conditions, crystalline BiOCl particles sensitised with Bi_2S_3 were also obtained, displaying similar diffraction patterns to those observed for samples A and E (ESI, Fig. S3†).

Thus the presence of H_2O is not a key determining factor in the synthesis and sensitisation of BiOCl–Bi_2S_3 particles in this medium and also does not justify the absence of particles when thiourea, thioacetamide and carbon disulphide were used.

The average BiOCl crystallite size was estimated from the XRD patterns by using the Scherrer equation. The obtained values were 7 ± 1 nm except for sample A with *ca.* 9 nm crystallite size. The XRD-derived values relate to the crystallite size within the nanoparticles and are thus smaller than the TEM-derived particle size values; the distinction is clear from inspection of the images in Fig. 3 (see below).

The morphology of the BiOCl particles decorated with Bi_2S_3 was analysed by TEM (Fig. 3). At low S concentration

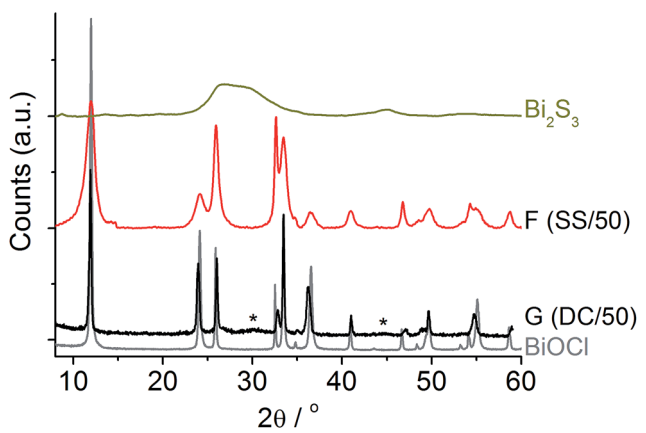

Fig. 2 XRD patterns of samples F (SS/50) and G (DC/50) and of pure BiOCl and nanoBi_2S_3.

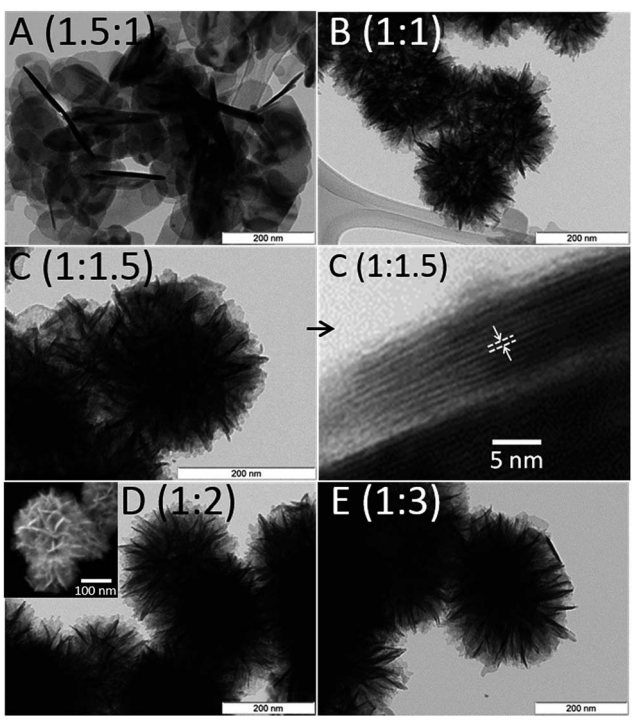

Fig. 3 TEM images of samples A (1.5 : 1), B (1 : 1), C (1 : 1.5), D (1 : 2) and E (1 : 3), and HRTEM image of sample C (1 : 1.5). Inset in figure: representative SEM image of sample D (1 : 2).

(sample A), plate-like particles are formed with average size of 59 ± 14 nm and 13 ± 4 nm thickness. When the sulphur concentration increases (samples B to E), flower-like hierarchical architectures of assembled nanosheets were formed with increasing diameter of 215, 221, 240 and 263 nm, respectively. These are composed of aggregated plates, as shown in the representative SEM image (inset in Fig. 3). The interlayer distance, obtained from HRTEM, is about 0.74 nm, as illustrated for sample C (1 : 1.5), in Fig. 3, which is consistent with the interlayer spacing between (001) planes of BiOCl (7.38 Å) and with the (001) preferential crystallographic orientation suggested by XRD analysis. Although it was not possible to estimate the Bi : S ratio in the nanoparticles by energy dispersive X-ray spectroscopy (EDX), since the Bi and S signals are overlaid in the energy scale, values ranging from 1.2 to 7.3 atom% of S were obtained by elemental analysis, confirming the presence of sulphur in the prepared samples. This indicates that $Na_2S_2O_3$ is a reliable source of sulphur for BiOCl sensitisation at room temperature. By using sodium sulphide as sulphur source, sample F (SS/50), the particles obtained are irregular size and shaped sheets of 51 ± 14 nm and thickness of about 10 ± 2 nm, similar to those prepared from sodium thiosulphate, sample A (1.5 : 1), despite the higher Bi : S ratio used (ESI, Fig. S4†). In the absence of water, sheet-like particles of about 46 ± 12 nm and 51 ± 12 nm were formed (ESI, Fig. S4†) for samples K (1 : 2) and L (1 : 4), similar to sample A. Although the Bi_2S_3 could be expected to present a thin sheet-like morphology (ESI, Fig. S5†), covering the surface of BiOCl as observed for the titanate nanofibers sensitised with Bi_2S_3 (ref. 34) or occur as small nanoparticles anchored to the BiOCl nanosheets,[27] in the present case, the *in situ* sensitisation by ion exchange, the small amount of Bi_2S_3 and its dispersity on the BiOCl surface did not allow its differentiation by TEM analysis in any of the prepared samples. Nevertheless its presence could be readily evidenced by XRD and DRS analysis.

Additionally, it can be concluded that the use of DES as the synthesis medium allows preparation of smaller particles with a more homogeneous particle size distribution than those of pure BiOCl and BiOCl–Bi_2S_3 prepared from aqueous medium, which are large and irregular sized and shaped plates (ESI, Fig. S5†). This effect may be a consequence of choline cation adsorption on the BiOCl particles in the initial stage of synthesis, controlling the growth of BiOCl nanostructures, since these particles, with (001) crystallographic surface orientation, are expected to have high surface density of oxygen atoms at the surface conferring a negative charge density and electric field perpendicular to the surface (see below).[6]

UV-vis optical response

The optical characterisation of the samples was carried out by measuring their diffuse reflectance, *R*, at room temperature, and the absorption spectra are depicted in Fig. 4a. The Bi_2S_3 sensitised BiOCl particles present contribution from both components and display two distinct absorption regions

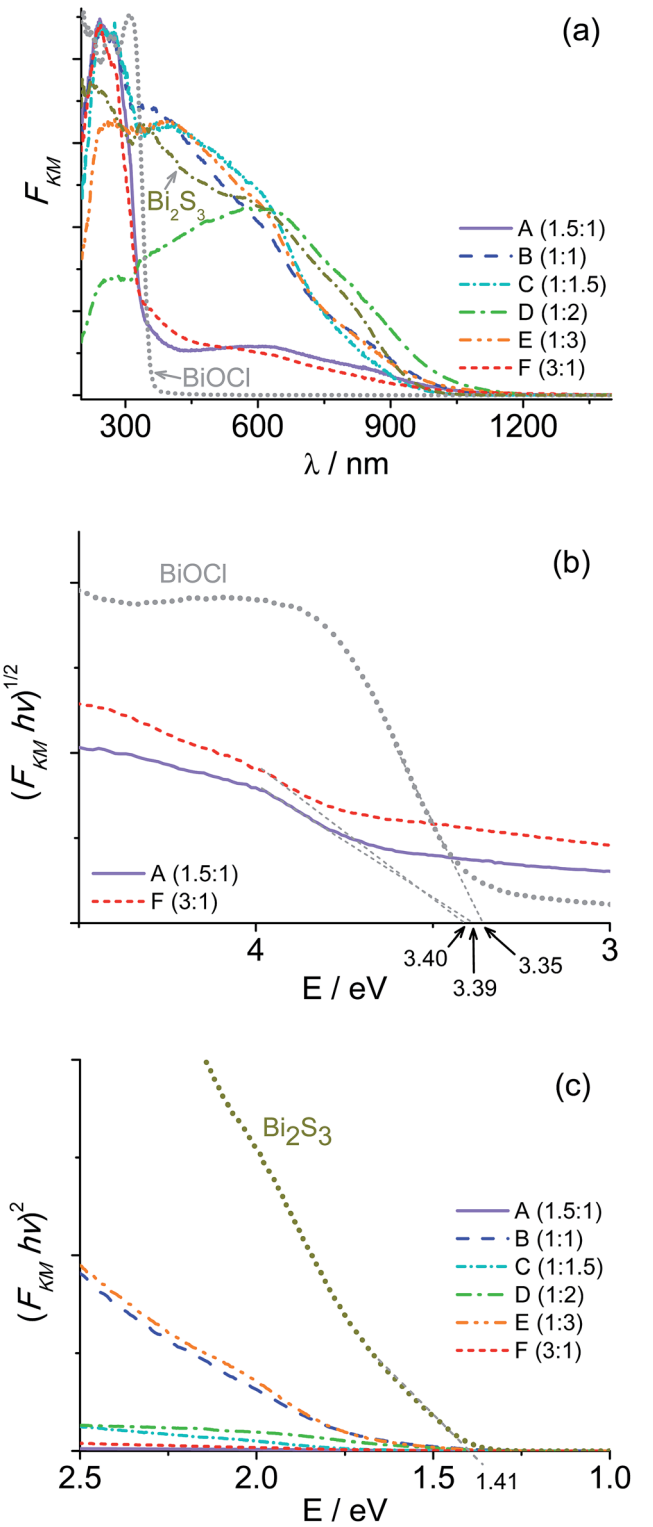

Fig. 4 (a) Diffuse reflectance spectra of Bi_2S_3–BiOCl samples A (1.5 : 1), B (1 : 1), C (1 : 1.5), D (1 : 2), E (1 : 3) and F (SS/50) and comparison with pure BiOCl and nanoBi_2S_3, (b and c) corresponding Tauc plots for the synthesised samples for indirect (b) and direct (c) transitions.

(Fig. 4). The pure BiOCl prepared absorbs in the UV region with the absorption edge at about 360 nm as shown in Fig. 4a. In contrast, the nanoBi_2S_3 absorbs across the entire UV-vis range.

The diffuse reflectance is related with the absorption Kubelka–Munk function, F_{KM}, through the relation $F_{KM}(R) = \frac{(1-R)^2}{2R}$, which is proportional to the absorption coefficient.[40] The optical band gap energies of the samples were estimated by plotting the function $f_{KM} = (F_{KM}h\nu)^n$ *vs.* radiation energy (Tauc plot), where h is the Planck constant and ν the radiation frequency and $n = 2$ or 1/2 for direct and indirect transitions, respectively. The E_g values were obtained by extrapolating the linear portion of the curve near the band edge to zero absorption (Fig. 4b and c). In Table 2 are included the E_g values obtained for the prepared samples considering the generally accepted indirect band gap for BiOCl[6,9,16,21,26] and direct band gap for Bi_2S_3.[26,41]

In samples A and F the relative contribution from BiOCl and Bi_2S_3, which have distinct E_g values (3.35 and 1.41 eV, respectively), could be distinguished. In contrast, for the nanoparticulates prepared with increasing proportion of sulphur in the reaction medium, the higher proportion of Bi_2S_3 on the resulting material did not allow that discrimination.

Regarding the contribution from the bismuth oxychloride, the optical band gap energies of samples A and F are clearly blue shifted relative to the pure BiOCl sample, in agreement with the quantum confinement effects.[42] Consequently, the blue shift of the optical band gap deduced for samples A and F seems to result from the differences in particle thickness which corroborates a decrease in particles size (thickness) for those prepared from DES and aqueous medium as revealed by the TEM images analysis. Regarding the bismuth sulphide contribution, the optical band gap energy of all samples is within the range of that obtained for nanoBi_2S_3 (1.41 eV) showing a small blue shift particularly for those samples with higher ratio of the sensitisation material. Moreover, these results seems consistent with the hypothesis that the Bi_2S_3 is not homogeneously distributed on the surface of BiOCl structures, and thus giving rise to two distinct optical band gap energies.

As the results presented above suggest, the optical band gap energy is related to the nanocrystal size. This effect can be described through the particle-in-a-box model, in which case the electron–hole pair is treated as a particle in a box with an infinite potential at the interface. For semiconducting nanoparticles with anisotropic growth the following equation can be applied:[43,44]

$$\Delta E \cong \frac{h^2\pi^2}{2\,\mu_{xy}}\left[\frac{1}{{L_x}^2}+\frac{1}{{L_y}^2}\right]+\frac{h^2\pi^2}{2\,\mu_z}\left[\frac{1}{{L_z}^2}\right]$$

relating the dimension, L_i, with the shift in the band gap energy, ΔE. Here ΔE is the difference of E_g between the bulk material and the nanomaterial ($\Delta E = E_{bulk} - E_g$), x and y are the coordinates of the lamellar plan of the particle, z the coordinate perpendicular to the lamellar plan, μ_i are the effective masses of the electron–hole (m_e^*, m_h^*) pair for the material in the plane xy, L_i is the particle dimension in the direction i and h is Planck's constant.

In the case of sheet-like particles two of their dimensions (x, y) are much larger than the third (z) which determines the material properties and is responsible for the confinement. Therefore, the synthesised particles for which it was possible to estimate the E_g values from the BiOCl contribution, samples A and F in Table 2, the sheet thickness was estimated using the equation above, the electron and hole masses of $0.56m_e$ and $1.10m_e$,[2] respectively, and the E_g shift observed between pure BiOCl and BiOCl–Bi_2S_3. Thicknesses of about 16 and 13 nm were respectively inferred which are close to those obtained directly from TEM images (13 ± 4 and 10 ± 2 nm, see above).

Table 2 Optical band gap energy (E_g) values of prepared samples

Sample		E_g/eV	
BiOCl		3.35	
nanoBi_2S_3			1.41
BiOCl–Bi_2S_3	A	3.39	1.33
	B		1.69
	C		1.72
	D		1.36
	E		1.71
	F	3.40	1.60
	G		1.65

RhB removal studies

In order to evaluate the ability of the synthesised materials to remove contaminants from aqueous solutions, two samples (B and F) were selected due to their distinct Bi_2S_3 : BiOCl ratio and morphology. Sample B presents a hierarchical structure of thin BiOCl–Bi_2S_3 sheets assembled in a flower-like morphology and higher Bi_2S_3 : BiOCl ratio, whereas sample F is formed by BiOCl–Bi_2S_3 sheets with average size of 51 nm and 10 nm thick. Rhodamine B (RhB) was used as model pollutant and its adsorption and photocatalytic degradation studied. Rhodamine B is a cationic dye which has been extensively used for photocatalytic activity evaluation of photocatalytically active materials and has been selected to be used as a model molecule/pollutant.

Adsorption studies. After 1 hour in the dark conditions for adsorption/desorption equilibrium, it was found that sample F has a much higher ability to adsorb RhB (49%, 30.7 mg g^{-1}) than sample B (34%, 22.2 mg g^{-1}), whereas pure BiOCl and nanoBi_2S_3 present low adsorption capacity, 15 and 22%, respectively (Table 3). These values are remarkable compared with those reported in the literature for BiOCl particles sensitised with Bi_2S_3, up to 2.6 mg g^{-1} for RhB adsorption on 2D BiOCl nanoplates[10] and 0.2 to 1.75 mg g^{-1} for MO adsorption on BiOCl nanostructures.[5,6]

Three hypothesis have been considered in order to clarify the origin of the high adsorption ability of these materials: (i) surface area, (ii) surface charge of the particles and/or (iii) insertion of RhB molecules in the interlayer spacing of the BiOCl structure.

The surface area measurements were performed by the Brunauer–Emmett–Teller (B.E.T.) method and 34.0 and 22.5 m^2 g^{-1} were obtained for samples B and F, respectively. For pure BiOCl and nanoBi_2S_3, values of 6.730 and 24.426 m^2 g^{-1}, respectively, were found. The results show that higher amount

Table 3 Amount of RhB adsorbed on samples B and F, surface area of the particles ($A_{B.E.T.}$), area occupied by adsorbed RhB with perpendicular ($A_{RhB\perp}$) and flat ($A_{RhB//}$) orientation on the surface and potential of zero charge (p.z.c.) of particles surface[a]

Sample	% RhB ads	(m_{RhB}/m_{NPs})/mg g^{-1}	$A_{B.E.T.}$/m^2 g^{-1}	$A_{RhB\perp}/A_{NPs}$	$A_{RhB//}/A_{NPs}$	p.z.c.
B	34	22.2	33.993	0.6	1.2	4.0
F	49	30.7	22.532	1.2	2.5	6.4
BiOCl	15	10.6	6.730	1.4	2.8	4.5
nanoBi_2S_3	22	15.4	24.426	0.6	1.2	—

[a] $\perp$ – perpendicular RhB molecule orientation with cationic group oriented towards the BiOCl surface; // – parallel orientation of RhB adsorbed flat on the BiOCl surface.

of RhB was adsorbed on smaller surface area of sample F (49%, 30.7 mg g^{-1}) than on sample B (34%, 22.2 mg g^{-1}). Therefore it could be concluded that the surface area was not the main effect controlling the adsorption capacity of these materials. Additionally, while nanoBi_2S_3 have higher surface area (fourfold) than that of pure BiOCl, the amount of RhB adsorbed on the former is about 1/3 of that adsorbed on the later, suggesting that in the hybrid structures it is the BiOCl component the main responsible for the dye adsorption.

Considering the effect of the surface charge, the point of zero charge (p.z.c.) of those materials was evaluated (Table 3) and compared with that of pure BiOCl (p.z.c. at pH < 2), which agrees with that reported in the literature (p.z.c. at pH ≈ 2).[11] As mentioned before, the surface of BiOCl nanostructures with (001) preferential crystallographic orientation are expected to have a high density of oxygen atoms on the surface and an electric field perpendicular to the surface[6] responsible for negative zeta potential in a wide range of pH values (pH > 2) and for the high affinity towards positively charged species.

Moreover, taking into account the pH of the RhB solution (pH 6.65) in this medium, the BiOCl–Bi_2S_3 particles surface is negatively charged and consequently the interaction with the zwitterionic molecule of RhB (chemical structure shown in Scheme 1) at this pH (pK_a 3.7) may occur through the positively charged –N$(CH_2CH_3)_2$ group. Furthermore, the particles with p.z.c. close to the pH of the solution and therefore less negatively charged in the RhB solution (sample F) show higher ability to remove the dye. This suggests that repulsive interactions (with the –COO$^-$ group) may hinder the RhB adsorption. In fact, comparing the area occupied by the adsorbed RhB molecules in two limit orientations (perpendicular ($\perp$) and parallel (//) to the surface) the results (Table 3) suggest that on sample B the RhB may adsorb preferentially in a perpendicular orientation as observed in fluorinated TiO_2 particles and hexagonal $ZnIn_2S_4$.[45,46] In those studies it was suggested that the negative surface charge due to the high density of surface anionic sites directed the RhB adsorption and once this was established through one –N$(CH_2CH_3)_2$ group, the loss of resonance in the aromatic rings prevented the interaction with the second –N$(CH_2CH_3)_2$ functionality.[45,46] Therefore, it is reasonable to expect that in the present case the adsorption may occur with the cationic group oriented to the surface and the deprotonated carboxylic acid group towards the solution. However, on sample F, which is less negatively charged at pH 6.65, the formation of multilayers in a flat or perpendicular orientation is more likely to occur. This may occur by both electrostatic interactions and π-stacking between aromatic rings.[47] The hypothesis of insertion of RhB molecules (thickness 4.75 Å, ACD/ChemSketch) in the interlayer spacing of the BiOCl structure ($d = 7.38$ Å), in a similar way to that previously reported for Rh6G intercalation in titanate nanotubes[48] has been discarded due to the zwitterionic nature of the molecules and since it was not observed any shift in the XRD peak corresponding to the interlayer spacing $2\theta = 12°$ (data not shown).

The results presented above indicate that the removal ability of such materials can be manipulated by changing the pH of the dye solution (to an extent limited by the dye properties) and the remarkable ability to remove RhB from solution by adsorption may also be expected to be extended to other cationic and anionic dyes by tuning the p.z.c. and adequate selection of the BiOCl–Bi_2S_3 heterostructures.

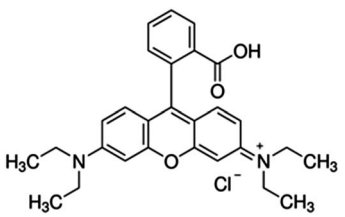

Scheme 1 Rhodamine B structure; pK_a (–COOH) = 3.7.

RhB photocatalytic degradation studies

RhB shows a strong absorption band at 554 nm which has been used to quantify the amount of adsorbed RhB and monitor the degradation process. In Fig. 5 are illustrated the UV-visible spectra obtained at different times during the degradation process of RhB using samples B and F as photocatalysts after adsorption/desorption equilibration in the dark for 1 h. The absorption band at 554 nm decreases once the irradiation was started. After *ca.* 45 min complete degradation of the dye was achieved using sample B as photocatalyst. By using sample F, fast degradation of RhB was observed and after 15 min of irradiation that band disappeared indicating complete discoloration of the RhB but an absorption band at 262 nm corresponding to degradation by-products remains. Considering that the surface area of sample F is smaller than that of sample B (Table 3) we can conclude that the better

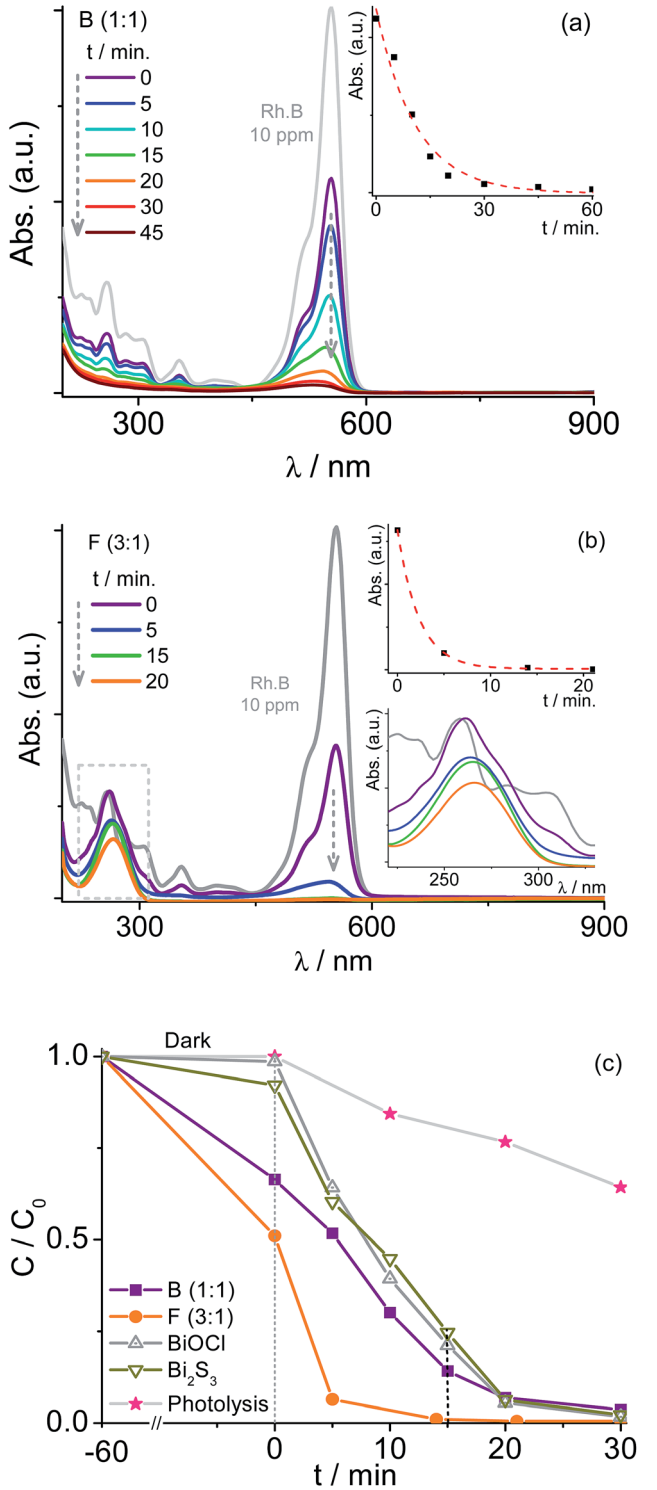

Fig. 5 Time profiles of adsorption and photocatalytic performance of samples B (a) and F (b) and comparison with pure BiOCl, nanoBi_2S_3 and photolysis responses (c), for RhB degradation under UV-visible light irradiation after 1 h in the dark.

photocatalytic activity of such particles is not due to its surface area. Enhanced photocatalytic efficiency was obtained for the sample with the lower relative proportion of Bi_2S_3, which is most probably due to extension of the absorption in the visible region without blocking too much the access of RhB to the BiOCl surface. Moreover, the remarkable photocatalytic activity of BiOCl nanoparticles sensitised with small proportion of Bi_2S_3 was achieved and full discoloration of RhB from aqueous solution was attained in a proportion of 75 mg of RhB per gram of catalyst. This result represents a significant improvement as compared with previously studies reported in the literature.[4,9,10,25,26]

The pure nanoBi_2S_3 and BiOCl samples were less efficient to the RhB photodegradation than samples B and F, and after 15 min of irradiation (Fig. 5) have degraded only 75 and 79% of the initial RhB in solution, respectively.

Under UV-visible irradiation the RhB degradation process onto the prepared composite nanostructures can follow two distinct mechanisms that are showed in Scheme 2. (i) Indirect dye photosensitisation under visible light irradiation for pristine BiOCl which is not excited under visible light; the photogenerated electron is transferred from the excited dye* to the conduction band (CB) of the catalyst, where the reaction with O_2 generates radical active species that are involved in the dye degradation process. (ii) Direct semiconductor photoexcitation under visible (Bi_2S_3) and UV light (BiOCl and Bi_2S_3) in which the electrons in the CB and the holes in the valence band (VB) are responsible for the generation of the radical active species (*e.g.* $^{\bullet}HO$ and $^{\bullet}O_2^-$). The hypothesis of direct semiconductor excitation involving charge carriers transfer from the CB of $Bi_2S_3$to the CB of BiOCl was further confirmed by photodegradation of RhB under visible light irradiation (Fig. 6). For clarity purposes, the absorbance data was normalised to $t = 0$ minutes (start of irradiation) and consequently the observed kinetic behaviour only takes into account the photodegradation process. By plotting $-\ln(C/C_0)$ *vs.* t, where C and C_0 are the RhB concentrations at $t = 0$ and $t = t$, the pseudo-first order rate constant, k, can be retrieved from the equation $-\ln(C/C_0) = kt$. Under these experimental conditions, using only visible radiation, but using

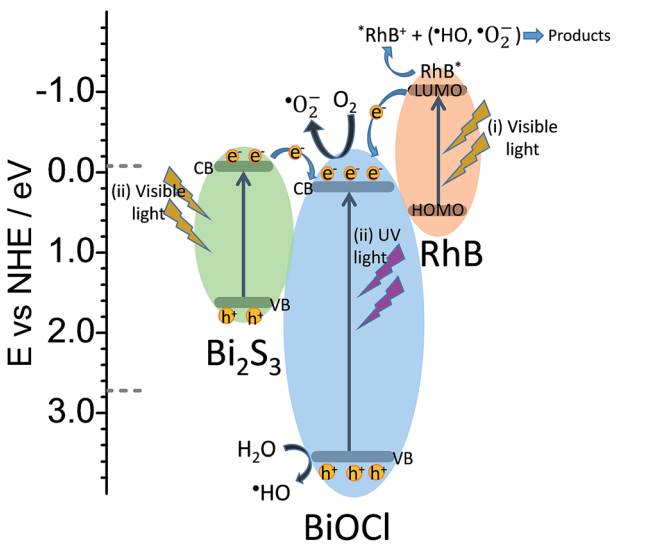

Scheme 2 Suggested energy diagram for the charge separation process for BiOCl–Bi_2S_3 composite and the degradation of RhB under UV-visible irradiation.

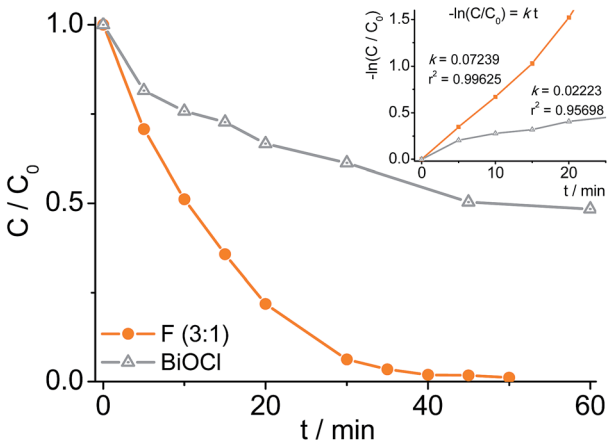

Fig. 6 Photocatalytic performance of sample F and pure BiOCl, for the RhB degradation under visible light irradiation.

BiOCl as catalyst, no photoexcitation occurs and very slow kinetics was observed ($k = 1.3\ h^{-1}$). On the other hand, by using the BiOCl–Bi_2S_3 composite (sample F) a 3 fold increase in the pseudo first-order rate constant was observed ($k = 4.3\ h^{-1}$). This significant enhancement of the rate constant in the presence of Bi_2S_3 on the BiOCl surface can only be assigned to the effective electron transfer within the composite material between the CB of Bi_2S_3 and the CB of BiOCl as theorised and depicted in Scheme 2, since the latter cannot be photoexcited by visible light.

Bearing in mind the E_g values for samples B and F and nanoBi_2S_3 and BiOCl (Table 2), the edge potential of the valence (VB) and conduction (CB) bands were estimated according to the equations[25,27] $E_{VB} = X - E^e + 0.5E_g$ and $E_{CB} = E_{VB} + E_g$, assuming the electronegativity of the semiconductors, X, of 6.36 and 5.27 for BiOCl and Bi_2S_3, respectively (Table 4). The VB and CB values obtained are close to those reported in the literature for BiOCl (3.5–3.6 and 0.14–0.22 eV) and Bi_2S_3 (1.44–1.47 and 0.09–0.11 eV).[18,25,27,49]

Additionally, it has been reported that for RhB the electronic transition occurs between the HOMO and HOMO−1 levels with an energy difference of about 1.42 eV.[49]

It is well known that the low recombination rate is a key factor in the photocatalyst efficiency and therefore the introduction of additional transition states by sensitisation is advantageous.[10,21]

Table 4 Band energy position for samples B and F and for pure BiOCl and nanoBi_2S_3

			E/eV	
Sample		X	VB	CB
BiOCl		6.36	3.54	0.18
nanoBi_2S_3		5.27	1.48	0.07
B	Bi_2S_3		1.62	−0.08
F	BiOCl		3.56	0.16
	Bi_2S_3		1.57	−0.03

Furthermore, the strong adsorption of RhB onto this material, prior to photodegradation, may function as an organic dye pre-sensitisation step and therefore contribute to the high photocatalytic performance.[10,11,18,21]

Although it has not been the main subject of this study, an absorption band at about 262 nm remained after 20 min of irradiation when using sample F as photocatalyst (inset in Fig. 5c). In fact, contrarily to the observed with sample B, this absorption band could be already clearly noticed after the equilibration time in the dark period ($t = 0$ in Fig. 5b), remaining throughout the degradation process. Additionally, this band is very likely to be from water soluble degradation products containing one aromatic ring and will be further discussed in a more detailed work. While this fact is regularly neglected due to the narrow wavelength interval commonly reported which frequently excludes the λ values ≤400 nm, a similar effect has been reported by Zheng *et al.*[50] for Rh6G and also observed for RhB but no further interpretation has been conveyed.[51] In the case of Rh6G it has been attributed to the deamination (and demethylation) of the dye and consequent conversion into an insoluble product. This has not been observed during the photodegradation of RhB onto sample F. By using sample B complete degradation is achieved and no absorption bands were detected at the end of the irradiation.

Comparing the two tested samples, although sample F shows enhanced ability to remove RhB from solutions and better photocatalytic activity, sample B allows complete degradation of RhB in solution without aromatic intermediary products. At the end of the photo-irradiation experiments, the stability of the catalysts was evaluated by XRD analysis. The diffraction patterns (ESI, Fig. S6†) show only a small increase in the crystallinity of the particulates after 1 h of irradiation with UV-vis light during RhB degradation, suggesting that these materials are feasible to be reused in repetitive degradation cycles. Therefore, homogeneous, crystalline, stable and photoactive Bi_2S_3-sensitised BiOCl catalysts can be successfully prepared in a one-pot approach at room temperature from environmentally friend deep eutectic solvent medium based on choline chloride and ethylene glycol.

Conclusions

An easy one-pot, room temperature synthesis of crystalline BiOCl particles sensitised with Bi_2S_3 has been successfully achieved. The obtained particles shape, aggregation degree (loose sheets or flower-like aggregates) and size could be controlled by the synthesis conditions. The effective sensitisation of BiOCl nanostructures with Bi_2S_3, was attained by a simultaneous *in situ* ion-exchange process, using different sulphur precursors, and the relative amount of Bi_2S_3–BiOCl controlled by the reactants (Bi : S) ratio in the synthesis medium. The resulting hybrid crystalline nanostructures show improved optical properties as compared with its individual components, extending the photoactive region of pure BiOCl to the visible range due to Bi_2S_3 sensitisation.

The BiOCl–Bi_2S_3 nanocomposite prepared using sodium thiosulfate allows complete degradation of RhB dye under

UV-visible light irradiation whereas those prepared from sodium sulphide precursor yield intermediary products, resulting in incomplete degradation of the dye molecules.

The combination of adsorption and photocatalytic activity enable swift removal of RhB from aqueous medium by adsorption and later recovery of catalyst by photodegradation of the adsorbed pollutant.

Acknowledgements

The authors gratefully acknowledge the financial support from Fundação para a Ciência e a Tecnologia (SFRH/BPD/77404/2011 and UID/MULTI/00612/2013). M. C. Neves acknowledges FCT for a post-doctoral grant (SFRH/BPD/110423/2015) and UID/CTM/50011/2013.

Notes and references

1 Z. Jiang, Y. Liu, T. Jing, B. Huang, Z. Wang, X. Zhang, X. Qin and Y. Dai, *RSC Adv.*, 2015, **5**, 47261.
2 X. Zhang, B. Li, J. Wang, Y. Yuan, Q. Zhang, Z. Gao, L.-M. Liu and L. Chen, *Phys. Chem. Chem. Phys.*, 2014, **16**, 25854.
3 L. Zhang, Z. Han, W. Wang, X. Li, Y. Su, D. Jiang, X. Lei and S. Sun, *Chem.–Eur. J.*, 2015, **21**, 18089.
4 K. Zhang, J. Liang, S. Wang, J. Liu, K. Ren, X. Zheng, H. Luo, Y. Peng, X. Zuo, X. Bo, J. Li and X. Yu, *Cryst. Growth Des.*, 2012, **12**, 793.
5 X. Hu, Y. Xu, H. Zhu, F. Hua and S. Zhu, *Mater. Sci. Semicond. Process.*, 2016, **41**, 12.
6 J. Jiang, K. Zhao, X. Xiao and L. Zhang, *J. Am. Chem. Soc.*, 2012, **134**, 4473.
7 Y. Lai, G. Wang, S. Song, W. Fan and H. Zhang, *CrystEngComm*, 2009, **11**, 1857.
8 L. Ding, H. Chen, Q. Wang, T. Zhou, Q. Jiang, Y. Yuan, J. Li and J. Hu, *Chem. Commun.*, 2016, **52**, 994.
9 Y. Li, Y. Tiang, R. Zhang, L. Ma, C. Zhou and X. Tian, *Inorg. Chim. Acta*, 2016, **439**, 123.
10 J. Xiong, G. Cheng, G. Li, F. Qin and R. Chen, *RSC Adv.*, 2011, **1**, 1542.
11 H. Zhao, Y. Zhang, G. Li, F. Tian, H. Tang and R. Chen, *RSC Adv.*, 2016, **6**, 7772.
12 M. Li, J. Zhang, H. Gao, F. Li, S.-E. Lindquist, N. Wu and R. Wang, *ACS Appl. Mater. Interfaces*, 2016, **8**, 6662.
13 J. Yuan, J. Wang, Y. She, J. Hu, P. Tao, F. Lv, Z. Lu and Y. Gu, *J. Power Sources*, 2014, **263**, 37.
14 Y. Zhang, S. Lu, M.-Q. Wang, Y. Niu, S. Liu, Y. Li, X. Wu, S.-J. Bao and M. Xu, *Mater. Lett.*, 2016, **178**, 44.
15 L. Ye, L. Zan, L. Tian, T. Peng and J. Zhang, *Chem. Commun.*, 2011, **47**, 6951.
16 M. Sun, Q. Zhao, C. Du and Z. Liu, *RSC Adv.*, 2015, **5**, 22740.
17 Y. Yu, C. Cao, H. Liu, P. Li, F. Wei and Y. Jiang, *J. Mater. Chem. A*, 2014, **2**, 1677.
18 C. Tan, G. Zhu, M. Hojamberdiev, K. Okada and J. Liang, *Appl. Catal., B*, 2014, **152–153**, 425.
19 M. Gao, D. Zhang, H. Li, X. Pu, X. Shao and W. Li, *Mater. Lett.*, 2015, **159**, 406.
20 L. Ding, C. Zhang, Q. Jiang, H. Chen, W. Sun and J. Hu, *Mater. Lett.*, 2015, **158**, 229.
21 G. Li, B. Jiang, S. Xiao, Z. Lian, D. Zhang, J. C. Yu and H. Li, *Environ. Sci.: Processes Impacts*, 2014, **16**, 1975.
22 S. Shamaila, A. K. L. Sajjad, F. Chen and J. Zhang, *J. Colloid Interface Sci.*, 2011, **356**, 465.
23 L. Zhang, W. Wang, L. Zhou, M. Shang and S. Sun, *Appl. Catal., B*, 2009, **90**, 458.
24 S. Y. Chai, Y. J. Kim, M. H. Jung, A. K. Chakraborty, D. Jung and W. I. Lee, *J. Catal.*, 2009, **262**, 144.
25 J. Cao, B. Xu, H. Lin, B. Luo and S. Chen, *Catal. Commun.*, 2012, **26**, 204.
26 S. Jiang, K. Zhou, Y. Shi, S. Lo, H. Xu and Y. Hu, *Appl. Surf. Sci.*, 2014, **290**, 313.
27 H. Cheng, B. Huang, X. Qin, X. Zhang and Y. Dai, *Chem. Commun.*, 2012, **48**, 97.
28 J. Huang, H. Zhang, X. Zhou and X. Zhong, *Mater. Chem. Phys.*, 2013, **138**, 755.
29 T. Wu, X. Zhou, H. Zhang and X. Zhong, *Nano Res.*, 2010, **3**, 379.
30 R. Albuquerque, M. C. Neves, M. H. Mendonca, T. Trindade and O. C. Monteiro, *Colloids Surf., A*, 2008, **328**, 107.
31 R. Piras, M. Aresti, M. Saba, D. Marongiu, G. Mula, F. Quochi, A. Mura, C. Cannas, M. Mureddu, A. Ardu, G. Ennas, V. Calzia, A. Mattoni, A. Musinu and G. Bongiovanni, *J. Phys.: Conf. Ser.*, 2014, **566**, 012017.
32 H. Yu, H. Bao, K. Zhao, Z. Du, H. Zhang and X. Zhong, *J. Phys. Chem. C*, 2014, **118**, 16602.
33 J. F. Cabrita, V. C. Ferreira and O. C. Monteiro, *Electrochim. Acta*, 2014, **135**, 121.
34 O. C. Monteiro and T. Trindade, *J. Mater. Sci. Lett.*, 2000, **19**, 859.
35 O. C. Monteiro, H. I. S. Nogueira, T. Trindade and M. Motevalli, *Chem. Mater.*, 2001, **13**, 2103.
36 A. R. Hillman, K. S. Ryder, C. J. Zaleski, V. Ferreira, C. A. Beasley and E. Vieil, *Electrochim. Acta*, 2014, **135**, 42.
37 H. Zhang, J. Huang, X. Zhou and X. Zhong, *Inorg. Chem.*, 2011, **50**, 7729.
38 T. J. Entradas, J. F. Cabrita, B. Barrocas, M. R. Nunes, A. J. Silvestre and O. C. Monteiro, *Mater. Res. Bull.*, 2015, **72**, 20.
39 X. Xiao, R. Hao, M. Liang, X. Zuo, J. Nan, L. Li and W. Zhang, *J. Hazard. Mater.*, 2012, **233–234**, 122.
40 V. C. Ferreira, M. R. Nunes, A. J. Silvestre and O. C. Monteiro, *Mater. Chem. Phys.*, 2013, **142**, 355.
41 O. C. Monteiro, T. Trindade, J.-H. Park and P. O'Brien, *Mater. Lett.*, 2003, **58**, 119.
42 G. Xi and J. Ye, *Inorg. Chem.*, 2010, **49**, 2302.
43 C. J. Sandroff, D. M. Hwang and W. M. Chung, *Phys. Rev. B: Condens. Matter Mater. Phys.*, 1986, **33**, 5953.
44 L. Sun, Z. Lin, J. Peng, J. Weng, Y. Huang and Z. Luo, *Sci. Rep.*, 2014, **4**, 4794.
45 Q. Wang, C. Chen, D. Zhao, W. Ma and J. Zhao, *Langmuir*, 2008, **24**, 7338.
46 Y. Chen, R. Huang, D. Chen, Y. Wang, W. Liu, X. Li and Z. Li, *ACS Appl. Mater. Interfaces*, 2012, **4**, 2273.

47 I. Moreno-Villoslada, M. Jofré, V. Miranda, P. Chandía, R. González, S. Hess, B. L. Rivas, C. Elvira, J. San Román, T. Shibue and H. Nishide, *Polymer*, 2006, **47**, 6496.
48 V. C. Ferreira and O. C. Monteiro, *J. Nanopart. Res.*, 2013, **15**, 1923.
49 M. A. Gondal, X. Chang, A. A. Al-Saadi, Z. H. Yamani, J. Zhang and G. Ji, *J. Environ. Sci. Health, Part A: Toxic/Hazard. Subst. Environ. Eng.*, 2012, **47**, 1192.
50 Y.-M. Zheng, R. F. Yunus, K. G. N. Nanayakkara and J. P. Chen, *Ind. Eng. Chem. Res.*, 2012, **51**, 5953.
51 H. A. Mallah, D. M. Naoufal, A. I. Safa and M. M. El Jamal, *Port. Electrochim. Acta*, 2013, **31**, 185.